Research Square

Preprints are preliminary reports that have not undergone peer review.
They should not be considered conclusive, used to inform clinical practice,
or referenced by the media as validated information.

Phase-history-addressed Josephson memory through an atomically thin antiferromagnet

Faxian Xiu

faxian@fudan.edu.cn

Department of Physics, Fudan University https://orcid.org/0000-0003-2860-0369

Linfeng Ai

Department of Physics, Fudan University

Yuda Zhang

Fudan University

Qiang Ma

Fudan University

Yuqiang Fang

Shanghai Jiaotong University

Xue-Jian Gao

Hong Kong University of Science and Technology https://orcid.org/0000-0003-4436-6584

Yitao Liu

Department of Physics, Fudan University

Changlin Zheng

Fudan University https://orcid.org/0000-0002-3030-9557

Hua Jiang

Fudan University https://orcid.org/0000-0002-8626-735X

Kam Tuen Law

The Hong Kong University of Science and Technology https://orcid.org/0000-0003-0501-6290

Fuqiang Huang

School of Materials Science and Engineering, Shanghai Jiao Tong University https://orcid.org/0000-0003-0526-5473

X. C. Xie

Fudan University

Article

Keywords:

Posted Date: November 18th, 2026

DOI: https://doi.org/10.21203/rs.3.rs-11687627/v1

License: This work is licensed under a Creative Commons Attribution 4.0 International License.
Read Full License

Additional Declarations: There is **NO** Competing Interest.

Phase-history-addressed Josephson memory through an atomically thin antiferromagnet

Linfeng Ai[1,2#], Yuda Zhang[1,2#], Qiang Ma[1,2], Yuqiang Fang[3], Xuejian Gao[4], Yitao Liu[1], Changlin Zheng[1], Hua Jiang[5], K. T. Law[4], Fuqiang Huang[3], X. C. Xie[5,6,7], Faxian Xiu[1,2,8*]

[1]State Key Laboratory of Surface Physics and Department of Physics, Fudan University, Shanghai 200433, China

[2]Institute for Nanoelectronic Devices and Quantum Computing, Fudan University, Shanghai 200433, China

[3]Key Laboratory of Intelligent Creation for Extreme Energy Materials of Ministry of Education, School of Materials Science and Engineering and Zhangjiang Institute for Advanced Study, Shanghai Jiao Tong University, Shanghai 200240, China

[4]Department of Physics, Hong Kong University of Science and Technology, Clear Water Bay, Hong Kong 999077, China

[5]Interdisciplinary Center for Theoretical Physics and Information Sciences (ICTPIS), Fudan University, Shanghai 200433, China

[6]International Center for Quantum Materials, School of Physics, Peking University, Beijing 100871, China

[7]Hefei National Laboratory, Hefei 230088, China

[8]Department of Physics, Shanghai University, Shanghai 200444, China

[#]These authors contributed equally to this work

*Correspondence should be addressed to F. X. (E-mail: Faxian@fudan.edu.cn).

Abstract

Integrating antiferromagnets into superconducting circuits combines sharp dissipationless-resistive switching with weak stray fields, promising high-density information processing, yet compact cryogenic memory cells remain elusive. Atomically thin antiferromagnets can serve as Josephson barriers that sustain supercurrent while retaining magnetic order, sculpting the junction's phase-energy landscape into addressable states for binary storage. Here we transform a Josephson rectifier into a superconducting phase memory in all-van der Waals $NbSe_2$/CrSBr/$NbSe_2$ junctions. CrSBr's in-plane magnetic anisotropy governs the training-induced reversal of zero-field Josephson diode polarity, while SQUID interferometry and half-integer Shapiro steps reveal a finite phase offset and strong higher-harmonic coupling, identifying the asymmetric, bistable Josephson potential underpinning the observed transport. Under a fixed magnetic preset, current history deterministically writes either phase state. Continuous microwaves exploit their unequal dynamical stability, rendering only the less confined state resistive and producing over 100-fold resistance contrast for non-destructive readout at zero DC bias, with the states remaining distinguishable for at least 6000 s. One weak link thus becomes a rewritable, magnetically programmable memory cell, establishing layered antiferromagnets as a materials platform for cryogenic superconducting circuits.

The development of quantum processors and single-flux-quantum logic circuits has intensified the need for compact, low-dissipation memory elements that operate natively at cryogenic temperatures[1,2], where conventional semiconductor memories impose substantial thermal overheads[3]. Superconducting circuits offer a natural platform for such memory, exploiting the sharp contrast between dissipationless and resistive transport for binary-state readout[4,5]. Complementing this readout capability, the macroscopic phase difference across a Josephson junction (JJ) provides an intrinsic degree of freedom for information storage[6,7]. Magnetic order offers a means to tailor Josephson coupling through exchange interactions and time-reversal-symmetry breaking[8–10]. These interactions can reshape the current-phase relation (CPR) and the associated Josephson energy landscape[11,12], where distinct minima can encode information in metastable phase states with distinguishable electrical responses[13–15]. Realizing this calls for a materials platform that links magnetic control of the phase landscape to electrical writing and readout in a compact Josephson device.

Van der Waals (vdW) heterostructures facilitate the integration of two-dimensional magnets with superconductors across atomically sharp and dangling-bond-free interfaces[16,17]. Studies of ferromagnetic vdW JJs have revealed nontrivial Josephson phase states associated with magnetic domain textures without deliberate barrier patterning[18–20], and demonstrated that magnetic training can reverse the polarity of the zero-field Josephson diode effect (JDE)[21]. Alongside these ferromagnetic systems, layered antiferromagnets with reduced net magnetization bring layer-dependent magnetic order into the Josephson weak link. Particularly attractive is CrSBr, an A-type antiferromagnetic semiconductor whose strong magnetic anisotropy and field-configurable spin arrangements[22–25] could enable magnetic-state-dependent Cooper-pair tunnelling. Its in-plane magnetic easy axis even permits direct field control of the spin configuration transverse to the vertical supercurrent. Whether such magnetic tunability can extend beyond supercurrent modulation to provide deterministic control of the Josephson phase response in functional devices remains an open question.

Here we incorporate this layered antiferromagnet in all-vdW $NbSe_2$/CrSBr/$NbSe_2$ JJs, combining magnetic control of superconducting rectification with history-dependent phase-state selection. Opposite magnetic presets reverse the zero-field JDE, whose angular dependence reveals the influence of intrinsic magnetic anisotropy of CrSBr on supercurrent non-reciprocity. At a fixed magnetic state, opposite current histories select two distinct finite-phase states, manifested as inequivalent switching branches, I_{c0} and I_{c-}, establishing phase-history addressing within a single junction. Superconducting-quantum-interference-device (SQUID) interferometry resolves an effective phase offset of $(0.58 \pm 0.11)\pi$ between these branches, while half-integer Shapiro steps reveal a substantial second-harmonic contribution ($|I_2/I_1| \approx 0.74\sim0.98$) to the CPR, together supporting an asymmetric bistable phase landscape. Both written states return to zero voltage after

removal of the write current, leaving their distinction hidden from conventional zero-bias transport. Microwave excitation makes this difference electrically visible by selectively destabilizing one state while preserving the superconducting response of the other, producing a significant resistance contrast for non-destructive readout without a DC bias. Repeated electrical writing reproducibly switches between the two outputs, which remain distinguishable for at least $6000\ \mathrm{s}$ after removal of the write current. By integrating magnetic presetting, electrical phase-state selection and microwave-assisted readout within a single vdW magnetic weak link, we realize a magnetically reconfigurable, phase-history-addressed Josephson memory.

Josephson phase design with magnetic order

The all-vdW JJs consist of a CrSBr magnetic barrier sandwiched between two 2H-$NbSe_2$ superconducting electrodes (Fig. 1a). The 2H-$NbSe_2$ comprises Se-Nb-Se layers with trigonal-prismatic coordination, stacked along the *c*-axis[26]. The devices are assembled by dry transfer[27] in an inert glovebox to minimize oxidation and interfacial degradation (Methods). This vertical architecture couples the magnetic order of CrSBr directly to the macroscopic phase difference $\Delta\varphi$ between the superconducting electrodes.

Effect of this coupling depends on the form of the Josephson potential. A conventional sinusoidal CPR yields a single minimum within each 2π period, whereas higher-harmonic contributions can reshape the potential into a double well. In the minimal two-harmonic model, $I_\mathrm{s} = I_1 \sin\varphi + I_2 \sin 2\varphi$, a sufficiently strong negative second harmonic ($|I_2/I_1| > 1/2$) produces two degenerate finite-phase minima, φ_- and φ_+ (Fig. 1b)[13]. The degeneracy of these minima can be further lifted by a magnetization-dependent anomalous contribution to the CPR, characterized by $I_\mathrm{a}(M)$. Under broken inversion ($\mathcal{P}$) and time-reversal ($\mathcal{T}$) symmetries, the interplay of exchange interaction and spin-orbit coupling (SOC) can generate such a contribution[12]. Combined with the higher harmonic, it can produce unequal critical currents in opposite directions, with the potential asymmetry[14,15] and thus the rectification polarity reversed by the remanent magnetization (Fig. 1c)[28–30]. For vertical transport, such non-reciprocity along $\mathbf{M} \times \nabla U$ is symmetry-allowed when the $\mathcal{P}$-asymmetry potential gradient ∇U has an in-plane component non-collinear with the magnetization $\mathbf{M}$.

CrSBr naturally hosts spontaneous in-plane spin order relevant to this phase control, with ferromagnetically aligned Cr moments within each layer and antiferromagnetic coupling between adjacent layers below its bulk Néel temperature ($T_\mathrm{Néel} \sim 133\ \mathrm{K}$)[22]. Its magnetic anisotropy further distinguishes the *b*-, *a*- and *c*-axes as the easy, intermediate and hard axes, respectively (Fig. 1d). At $T = 2\ \mathrm{K}$, the bulk magnetization changes abruptly along *b*, characteristic of a spin-flip transition, increases gradually through spin canting along *a* and saturates at substantially higher fields along *c* (Fig. 1e). These distinct magnetic responses are also reflected in a graphite/four layer-CrSBr/graphite tunnel junction at 1.9 K (Figs. 1f and 1g), suggesting that the spin responses are retained in atomically thin CrSBr. We next examine how this magnetic anisotropy influences supercurrent transport.

Magnetically reversible zero-field Josephson rectification

We first characterize the zero-field current-voltage (IV) response of the four-layer CrSBr-JJ device NCN-01 at 1.85 K following different magnetic-training histories (Fig. 2a). In the untrained state, the positive and negative switching currents, I_c^+ and I_c^-, are nearly equal in magnitude. Training at $+100$ mT along the CrSBr b-axis and returning to zero field yields $I_c^+ > |I_c^-|$, whereas training at -100 mT reverses this inequality. We quantify the rectification by $\eta_{\mathrm{JDE}} = |\Delta I_c/(I_c^+ + |I_c^-|)|$, where the sign of $\Delta I_c = I_c^+ - |I_c^-|$ determines the polarity. The efficiency η_{JDE} reaches 14.5% and 19.2% for the positive and negative field presets, respectively. The switching asymmetry weakens with increasing temperature (T) and is strongly suppressed near 3 K (Fig. 2b), well below the superconducting transition at $T_c \approx 6$ K. This separation of temperature scales indicates that the rectification is not governed simply by suppression of superconductivity. The switching asymmetry also translates into a reversible voltage output. Under a square-wave current bias, the rectified voltage reverses sign with the magnetic-training direction (Fig. 2c).

We next probe the finite-field Josephson response with an in-plane magnetic field ($\mu_0 H$) along the CrSBr b-axis. The interference patterns exhibit clear hysteresis between upward and downward field sweeps and approximately map onto each other under simultaneous reversal of current and field, $(I, H) \rightarrow (-I, -H)$ (Fig. 2d), linking the zero-field JDE to magnetic-field history. Similar behavior, including the evolution and eventual saturation of the switching asymmetry with increasing training field, is observed in junctions with different CrSBr thicknesses (Extended Data Fig. 1). Measurements across four individual JJs with four- to six-layer CrSBr (Extended Data Table 1) establish the reproducibility of the magnetically reversible zero-field JDE.

We further examine the crystallographic dependence of the zero-field JDE in device NCN-02. Compared with the nearly reciprocal untrained state, magnetic training at ± 120 mT along either in-plane axis produces polarity-reversible JDE, with a substantially stronger response along the CrSBr b-axis than along the a-axis (Fig. 2e). Rotating the training field from b ($\theta = 0°$) toward a ($\theta = 90°$) at the same field magnitude reveals an overall decrease in the magnitude of the diode efficiency for both magnetic presets (Fig. 2f). This trend reflects the intrinsic magnetic anisotropy of CrSBr in the zero-field Josephson rectification.

Taken together, these results identify the field-trained magnetic configuration as the $\mathcal{T}$-odd parameter governing the zero-field JDE polarity. The oppositely trained states approximately follow a generalized field-current reversal relation[31], $I_c^+(\mu_0 H, +M) \simeq -I_c^-(-\mu_0 H, -M)$. Both Zeeman and exchange fields should therefore be considered. The sizable JDE in both odd- and even-layer CrSBr junctions suggests that magnetic configurations other than the uncompensated layer magnetization of ideal odd-layer stacking may contribute, with their roles potentially differing between layer parities (Supplementary Section 6).

Current-history-addressed Josephson switching

At a fixed magnetic preset, current history provides a second means of controlling the Josephson response by selecting the occupied phase well and its corresponding switching branch[32]. Such phase-state selection can itself reverse the JDE polarity, as observed in 45°-twisted cuprate junctions with broken $\mathcal{T}$ symmetry[33]. Within the resistively and capacitively shunted junction (RCSJ) model[34], opposite write-current excursions tilt the bistable Josephson potential and can prepare two phase states, φ_- and φ_+, which remain occupied after the current bias returns to zero (Fig. 3a). Probing these states with both current polarities yields four switching branches, $I_{c0}^{\pm}$ and $I_{c-}^{\pm}$ (Fig. 3b). The superscript denotes the measurement polarity, whereas the subscript specifies whether the preceding current excursion follows the same (I_{c0}) or opposite (I_{c-}) direction.

We examine this behavior in device NCN-03, a mixed SQUID comprising a five-layer CrSBr-based JJ and a nonmagnetic $NbSe_2$ reference JJ, which is designed for subsequent phase-sensitive measurements. At 1.6 K, following opposite in-plane magnetic presets ($\pm M_{\parallel}$) along the CrSBr b-axis, the current-history-resolved IV characteristics exhibit distinct switching thresholds for both current polarities (Figs. 3c and 3d). The separation between the I_{c0} and I_{c-} branches persists under both magnetic configurations, while its dependence on current polarity changes with the magnetic preset (Fig. 3e).

Phase-sensitive evidence for a bistable Josephson landscape

We next exploit the mixed-SQUID geometry of NCN-03 to resolve the phase difference between the two current-history-selected states. Following in-plane magnetic training, SQUID interferometry is performed under an out-of-plane field, with the non-magnetic arm serving as a phase reference (Fig. 4a). A separate all-$NbSe_2$ SQUID on the same chip provides an independent field reference. After the $+M_{\parallel}$ preset at 1.6 K, the I_{c0}^{+} and I_{c-}^{+} oscillations of NCN-03 are displaced by approximately 0.04 mT (Fig. 4b). Fitting the interference patterns yields a relative phase difference of $\Delta\varphi_H = (0.58 \pm 0.11)\pi$, as detailed in Supplementary Section 7. The simultaneously measured all-$NbSe_2$ SQUID shows no comparable branch displacement, excluding a common shift of the field origin. Because local magnetic flux and loop screening may also contribute[35], we interpret the displacement as an effective interferometric phase offset, rather than an absolute ground-state phase shift.

At 3.5 K, opposite magnetic presets produce a separate shift of approximately 0.065 mT in the I_{c0} interference patterns (Fig. 4c), corresponding to $(0.95 \pm 0.06)\pi$. This magnetization-dependent offset is distinct from the history-dependent separation, which weakens with increasing temperature and becomes unresolved near 3.5 K (Supplementary Fig. 19). Over the same temperature range, the I_{c0} oscillations in the $+M_{\parallel}$ state show little displacement, suggesting that the trained phase state remains relatively stable.

A purely shifted sinusoidal CPR cannot, on its own, support two stable phase minima. To

describe the bistable Josephson potential and its magnetic asymmetry, we adopt the minimal phenomenological model, $I_s(\varphi, M) = I_1 \sin\varphi + I_2 \sin 2\varphi + I_a(M)\cos\varphi$, where $I_a(-M) = -I_a(M)$. The cosine term introduces a magnetization-dependent shift of the first harmonic, which, together with the second harmonic, can make the two minima inequivalent. We therefore probe the higher-harmonic contribution through microwave-driven Josephson transport. In NCN-03 after the $-M_{\parallel}$ preset, integer Shapiro steps dominate the IV characteristics at 1.6 K under microwave irradiation at $f = 10$ GHz and $P = 6$ dBm, whereas half-integer steps become clearly resolved at 3 K, particularly in its differential resistance ($\mathrm{d}V/\mathrm{d}I$) trace (Fig. 4d). Their frequency and power dependences (Extended Data Fig. 2) support fractional phase locking associated with a substantial second harmonic[8,13,36]. Analysis of the power-dependent step widths yields a semiquantitative range of $|I_2/I_1| \approx 0.74\sim0.98$ (Supplementary Section 8). Assuming a negative I_2, this range exceeds the bistability threshold of $1/2$ and corresponds to a separation of approximately $0.53\pi\sim0.66\pi$ between the phase minima in the symmetric limit, comparable to the history-dependent effective phase offset obtained from SQUID interferometry.

This AC response also retains a clear magnetic dependence. The $\mathrm{d}V/\mathrm{d}I$ spectra exhibit a bias-polarity asymmetry that reverses with $M_{\parallel}$, particularly near the half-integer steps (Figs. 4e and 4f). This behavior reflects the interplay between the magnetization-dependent anomalous term and the second harmonic term. Upon warming, the asymmetry weakens alongside the DC JDE, while the fractional steps become more discernible. The latter may result from an increased normalized microwave drive I_{RF}/I_c as I_c decreases, without necessarily implying an increase in $|I_2/I_1|$ (Supplementary Section 9).

Microwave-assisted readout of Josephson phase memory

The preceding measurements establish the phase characteristics and current-history-dependent switching of two addressable states within an asymmetric bistable Josephson potential. Although current excursions can write these states, distinguishing them still requires an IV sweep, motivating an alternative approach to electrical readout. Indeed, microwave irradiation markedly enhances the separation between the two switching branches. Under both $+M_{\parallel}$ and $-M_{\parallel}$ presets, the microwave drive suppresses I_{c0} much more strongly than I_{c-}, with the dominant bias polarity reversing upon magnetic training (Figs. 5a and 5b). We quantify the branch separation by $\Delta I_c = |I_{c-} - I_{c0}|$ (Fig. 5c) and the normalized contrast $\eta = |(I_{c-} - I_{c0})/I_{c-}|$ (Fig. 5d). Both quantities increase over an intermediate power range. At higher power, the absolute branch separation vanishes as both switching branches are suppressed. Near 8 dBm, I_{c0} is nearly extinguished while I_{c-} remains finite, yielding $\eta = 98.7\%$. More importantly, under the same irradiation, the two history-selected states exhibit sharply different resistances at zero DC bias, opening a route to easy readout.

To understand this branch-selective response, we examine the phase dynamics in the asymmetric bistable Josephson potential (Fig. 5e). Unlike Shapiro locking in the running state, microwave

excitation near zero DC bias can induce escape from a local phase minimum, depending on the stability of the occupied state. Within the minimal CPR model, the diode efficiencies of I_{c-} branches in the absence of microwave (2.3% and 2.6% for opposite magnetic presets) yield an estimated magnetization-odd phase shift of $|\delta| \approx 0.02\pi$ (Supplementary Section 10). This small shift barely changes the separation between the phase minima, but greatly alters their confinement. The local curvatures, $K_i = \partial^2 U/\partial\varphi^2|_{\varphi_i}$, differ by a factor of $K_{\mathrm{stiff}}/K_{\mathrm{soft}}\sim 1.31$, while the escape barriers to the intervening saddle differ by $\Delta U_{\mathrm{high}}/\Delta U_{\mathrm{low}}\sim 2.25$. Thus, even a small magnetic asymmetry can produce a substantial imbalance in phase-state stability.

Under microwave driving, this imbalance further translates into distinct escape thresholds for the two phase states. In the quasistatic limit, the softer and stiffer minima lose stability at normalized RF amplitudes of $I_{\mathrm{RF}}/I_1 \approx 0.16$ and 0.27, respectively. RCSJ simulations at $10\ \mathrm{GHz}$ preserve this ordering, yielding corresponding thresholds of approximately 0.19 and 0.30 (Supplementary Section 10). This separation explains the intermediate-power regime in which I_{c0} is nearly suppressed while I_{c-} remains finite, providing a dynamical basis for the microwave-enhanced branch contrast and subsequent phase-state readout.

This selectivity forms the basis of phase-history-addressed Josephson memory. In conventional Josephson rectification, the magnetic preset determines the rectification polarity, while a continuous alternating bias drives the voltage output. In our scheme, the magnetic preset similarly determines the mapping between write-current polarity and phase-state occupation. The key difference lies in the separation of writing and readout: a current excursion writes a retained phase state, which can subsequently be distinguished by microwave-assisted readout without a DC read bias. The rectification thus acquires a retained, electrically addressable state rather than a drive-sustained response.

We demonstrate this preset-write-retain-read sequence at $1.6\ \mathrm{K}$ under $10\ \mathrm{GHz}$ microwave irradiation (Fig. 5f). Following opposite write-current excursions in the $-M_{\parallel}$ state, a $0.1\ \mu\mathrm{A}$ AC probe distinguishes two zero-DC-bias resistance levels of approximately $2.4\ \Omega$ and $0.01\ \Omega$, yielding a readout contrast exceeding two orders of magnitude. Both states persist for at least $6000\ \mathrm{s}$ after a single write, while multiple alternating write cycles reproducibly switch between them without appreciable loss of contrast. Reversing the magnetic preset to the $+M_{\parallel}$ state interchanges the write-current polarities associated with the high- and low-resistance states (Extended Data Fig. 3). Without a DC read bias, repeated low-amplitude probing preserves the state distinction over the measured interval, avoiding a static tilt of the Josephson potential during readout.

Discussion and outlook

The stored degree of freedom here is local to the Josephson weak link. Once the remanent magnetic state is preset, the two phase states can be repeatedly rewritten through current history

without further magnetic-field modulation. This differs from representative phase-based memories in which state switching relies on magnetic field or flux control, including the selection of phase minima in a φ-junction[6], changes in winding number through flux-driven phase slips[7], and the injection or removal of Josephson vortices[37]. Here, the magnetic preset configures the phase landscape and its addressing polarity, and the switching between the two states is then achieved solely through electrical control.

The vdW platform is suited to this memory architecture because magnetic order and structural asymmetry can be incorporated directly through stacking. Inequivalent interfaces, asymmetric layer sequences or twist can break $\mathcal{P}$ symmetry[38,39], while layered magnets accommodate diverse spin configurations and field-driven spin evolutions. In CrSBr, the strong in-plane anisotropy also introduces directional dependence, as reflected in the angular JDE response shown above. Further measurements show substantial reconstruction of the Josephson interference patterns with increasing field excursions along the *b*-axis, whereas the oscillations remain more regular along the *a*-axis (Supplementary Fig. 8). These differences may be associated with abrupt spin flipping and gradual spin canting, respectively, suggesting the possibility of discrete or continuous tuning of the effective phase bias and Josephson potential through magnetic training.

As stated, both $\mathcal{P}$ and $\mathcal{T}$ symmetry breaking are required for the zero-field JDE, with several possible microscopic origins in our junctions. Cross-sectional high-angle annular dark-field scanning transmission electron microscopy (HAADF-STEM) reveals an approximately 0.5 nm-wide region of reduced intensity at the lower CrSBr/$NbSe_2$ interface (Supplementary Fig. 4), suggesting structural inequivalence between the two superconductor-magnet interfaces, while an in-plane component of ∇U is still needed for vertical non-reciprocal response[12]. Meanwhile, the intrinsic Ising SOC of $NbSe_2$ can couple to the in-plane exchange field of CrSBr through spin-dependent tunnelling[18], while interfacial Rashba-like SOC[40,41] may also contribute to the anomalous CPR. Zero-field JDE is also observed in junctions using 2M-WS_2 electrodes (Supplementary Section 3). On the magnetic side, field-trained antiferromagnetic domains and pinned domain walls, previously observed in few-layer CrSBr[42,43], represent another candidate source of remanent uncompensated moments in both even- and odd-layer junctions. After thermal cycling, a weak JDE with the trained polarity persists in the five-layer device, whereas the six-layer device returns to a nearly reciprocal response (Supplementary Fig. 15). Even in nominally compensated junctions, asymmetric interfacial exchange[44] and stray-field-assisted flux pinning[45,46] may introduce additional magnetic contributions to the supercurrent. The absence of detectable JDE in NCN-05 (Extended Data Fig. 4) further highlights the role of interfacial asymmetry alongside magnetic order to the required rectification.

Having established the architectural and materials basis of this phase-based memory, we finally turn to the specific role of microwave excitation. Recent microwave-driven Josephson rectifiers have exploited Shapiro dynamics to achieve perfect diode efficiency in current-trained twisted

$Bi_2Sr_2CaCu_2O_{8+x}$ junctions[47] and quantized zero-bias RF rectification in monolithic CsV_3Sb_5 weak-link devices[48]. In these systems, microwave irradiation directly participates in generating the rectified output, either by driving the diode towards the ideal limit or by selecting quantized voltage levels. In our device, the microwave neither writes nor defines the stored state. Instead, it amplifies the dynamical contrast between current-history-selected phase states, enabling distinct resistance levels without a certain read bias. Ideally, the low-resistance memory state should approach a dissipationless superconducting response. Nevertheless, the residual resistance observed here ($\sim 10^{-2}\ \Omega$) may partly arise from RF-driven dynamics. Optimizing towards higher normal-state resistance and lower critical current could enhance the readout contrast while reducing the required microwave drive, leaving scope for future improvements in junction design.

To conclude, we demonstrate magnetically reconfigurable and phase-history-addressed Josephson memory in all-vdW $NbSe_2$/CrSBr/$NbSe_2$ junctions, where the layered antiferromagnet CrSBr enables magnetic control of an asymmetric, bistable Josephson phase landscape. Its strong in-plane magnetic anisotropy governs the response to magnetic training, which reverses zero-field rectification and determines the polarity of electrical writing. Current history then selects persistent phase states, supported by phase-sensitive SQUID interferometry and a substantial higher-harmonic contribution to the CPR. Under continuous microwave excitation, their unequal dynamical stability translates into sharply contrasting resistances without a DC read bias, enabling repeated electrical write-retain-read operations under a fixed magnetic preset. More broadly, these results motivate the exploration of vdW heterostructures combining layered magnetism, polar or ferroelectric order, and twist-engineered unconventional superconductivity to tailor Josephson phase landscapes for superconducting memory.

Methods

Sample preparation. Single crystals of bulk 2H-$NbSe_2$ were grown using the chemical vapor transport method, employing iodine as the transport agent. A mixture of Nb and Se powders with 0.2% excess Se relative to the stoichiometric composition was sealed with 0.1 g in an evacuated quartz tube. The tube was then placed in a two-zone furnace with a temperature gradient from 730 ℃ to 770 ℃ for two weeks. Single crystals of CrSBr were purchased from HQ-Graphene. Single crystals of 2M-WS_2 were prepared by deintercalation of interlayer potassium cations from $K_{0.7}WS_2$ crystals. For the synthesis of $K_{0.7}WS_2$, K_2S_2 (prepared via liquid ammonia), W, and S powders were mixed in the stoichiometric ratios and ground in an argon-filled glovebox. The mixture was pressed into a pellet and sealed in an evacuated quartz tube. The tube was heated at 850 ℃ for 2000 min and then slowly cooled to 550 ℃ at a rate of 0.1 ℃ min^{-1}. The synthesized $K_{0.7}WS_2$ was chemically oxidized using $K_2Cr_2O_7$ in aqueous H_2SO_4 at room temperature for 1 h. Finally, the 2M-WS_2 crystals were washed several times with distilled water and dried in a vacuum oven at room temperature.

Device fabrication. The heterostructure devices were fabricated using a dry-transfer method in a glovebox with both H_2O and O_2 levels below 0.1 ppm. Flakes of 2H-$NbSe_2$, CrSBr, and 2M-WS_2 were mechanically exfoliated onto polydimethylsiloxane (PDMS) stamps, with their thicknesses roughly estimated by optical microscopy. Subsequently, they were stacked slowly onto a Si substrate capped with a 285 nm-thick SiO_2 layer, with the process controlled by a stepper motor. The complete stack was removed from the glovebox for electrode fabrication. The multi-terminal contacts were patterned using standard *e*-beam lithography, followed by deposition of Cr/Au (5/55 nm) via magnetron sputtering. To fabricate the mixed SQUID, the CrSBr flake was placed over part of the bottom $NbSe_2$ flake. The top $NbSe_2$ flake was then positioned across both the CrSBr-covered and uncovered regions. The SQUID geometry was defined by electron-beam lithography, and the unwanted regions were removed by reactive ion etching using a mixture of SF_6 and O_2.

Device morphology characterization. Atomic-resolution scanning transmission electron microscopy (STEM) imaging was performed on a double aberration-corrected field-emission transmission electron microscope (Thermo Fisher Scientific Themis Z) operated at 300 kV. High-angle annular dark field (HAADF) STEM images were acquired using a probe convergence semi-angle of 21.4 mrad and detector collection semi-angles of 79 - 200 mrad, while the energy dispersive X-ray spectroscopy (EDS) signals were collected with a Super-X G2 EDS detector. The thicknesses of the exfoliated materials were determined from step-height profiles using a Park Systems atomic force microscope (AFM) operated in non-contact mode. The flake morphology and boundaries were examined using a Raith scanning electron microscope (SEM) at an accelerating voltage of 5 kV. The resulting secondary-electron images were used to determine the lateral geometry of the samples.

Transport measurements. DC transport measurements were performed in a Physical Property

Measurement System (PPMS, Quantum Design) with a base temperature of 1.85 K and in an Oxford Instruments 12 T ^{3}He cryostat. Superconducting current-voltage characteristics and differential-resistance measurements were performed by combining a DC bias supplied by an Agilent 2902 source meter and a small AC excitation from a lock-in amplifier (SR830, Stanford Research Systems) through a series resistor. The lock-in excitation frequency was set to 17.77 Hz. The zero-DC-bias resistance measurements therefore refer to zero applied DC current while retaining this small-signal AC probe. For magneto-transport measurements, the magnetic field was mainly applied in the sample plane along the specified crystallographic direction of CrSBr, perpendicular to the out-of-plane transport current through the junction. For SQUID oscillation measurements, a Keithley 2400 source meter was used to supply a small current to generate the sensitive magnetic-field excitation.

For AC Josephson measurements, the microwave excitation was generated using a Ceyear 1466G analog signal generator, which provides ultra-low phase noise and high output power. A field emitter was placed near the sample to couple the AC field to the Josephson junction. DC transport and differential-resistance measurements were performed simultaneously under continuous microwave irradiation using the same DC-bias and lock-in detection scheme described above. For the zero-DC-bias readout used in the rectification tests, the AC current supplied by the lock-in amplifier for resistance readout was much smaller than the remaining switching current of the superconducting branch under the applied microwave conditions and did not drive the junction across its switching threshold. All microwave measurements were performed in a single cooldown to ensure parameter consistency. The microwave power was swept from low to high values to minimize hysteresis from thermal effects.

Data availability

The data that support the plots within this paper and other findings of this study are available from the corresponding author upon reasonable request.

Acknowledgements

F. X. is supported by the National Natural Science Foundation of China (52225207), the Shanghai Pilot Program for Basic Research - FuDan University 21TQ1400100 (21TQ006), and the Shanghai Municipal Science and Technology Major Project (Grant No. 2019SHZDZX01). X. C. X. acknowledges support from the National Natural Science Foundation of China (12634001). L. A. thanks Professor Yu Ye from Peking University for valuable discussions and Pengliang Leng, Zihan Li, Minhao Zhao, Zehao Jia, and Xiaoyi Xie for their assistance.

Author contributions

F.X. conceived the ideas and supervised the overall research. Y.F. and F.H. synthesized 2M-WS_2 bulk samples. Y.Z. synthesized 2H-$NbSe_2$ bulk samples. L.A., Y.Z., and Q.M. fabricated the nanodevices. L.A., Y.Z., and Q.M. performed the transport measurements and data analysis. L.A. and Y.Z. performed AFM, SEM, and SQUID magnetometry characterizations. Y.L. and C.Z. performed

the STEM measurements. X.G., K.T.L., H.J., and X.C.X. provided in-depth discussions on the superconductivity mechanism. X.G. provided in-depth discussions on the magnetic mechanism. L.A., Y.Z., Q.M., and F.X. analyzed and interpreted the results. L.A. and F.X. wrote the paper with assistance from all other co-authors.

Competing financial interests

The authors declare no competing financial interests.

References

1. Alam, S., Hossain, M. S., Srinivasa, S. R. & Aziz, A. Cryogenic memory technologies. *Nat. Electron.* **6**, 185–198 (2023).
2. Megrant, A. & Chen, Y. Scaling up superconducting quantum computers. *Nat. Electron.* **8**, 549–551 (2025).
3. Pauka, S. J. *et al.* A cryogenic CMOS chip for generating control signals for multiple qubits. *Nat. Electron.* **4**, 64–70 (2021).
4. Klein, D. R. *et al.* Electrical switching of a bistable moiré superconductor. *Nat. Nanotechnol.* **18**, 331–335 (2023).
5. Bhakat, S., Samanta, S., Mahapatra, S. & Pal, A. Bistable and absolute switching driven by superconducting exchange coupling. *Nat. Commun.* **16**, 9609 (2025).
6. Goldobin, E. *et al.* Memory cell based on a φ Josephson junction. *Appl. Phys. Lett.* **102**, 242602 (2013).
7. Ligato, N., Strambini, E., Paolucci, F. & Giazotto, F. Preliminary demonstration of a persistent Josephson phase-slip memory cell with topological protection. *Nat. Commun.* **12**, 5200 (2021).
8. Sellier, H., Baraduc, C., Lefloch, F. & Calemczuk, R. Half-integer Shapiro steps at the 0–π crossover of a ferromagnetic Josephson junction. *Phys. Rev. Lett.* **92**, 257005 (2004).
9. Baek, B., Rippard, W. H., Benz, S. P., Russek, S. E. & Dresselhaus, P. D. Hybrid superconducting-magnetic memory device using competing order parameters. *Nat. Commun.* **5**, 3888 (2014).
10. Gingrich, E. C. *et al.* Controllable 0–π Josephson junctions containing a ferromagnetic spin valve. *Nat. Phys.* **12**, 564–567 (2016).
11. Golubov, A. A., Kupriyanov, M. Yu. & Il'ichev, E. The current-phase relation in Josephson junctions. *Rev. Mod. Phys.* **76**, 411–469 (2004).
12. Buzdin, A. Direct coupling between magnetism and superconducting current in the Josephson φ_0 junction. *Phys. Rev. Lett.* **101**, 107005 (2008).
13. Goldobin, E., Koelle, D., Kleiner, R. & Buzdin, A. Josephson junctions with second harmonic in the current-phase relation: properties of φ junctions. *Phys. Rev. B* **76**, 224523 (2007).
14. Goldobin, E., Koelle, D., Kleiner, R. & Mints, R. G. Josephson junction with a magnetic-field tunable ground state. *Phys. Rev. Lett.* **107**, 227001 (2011).
15. Sickinger, H. *et al.* Experimental evidence of a φ Josephson junction. *Phys. Rev. Lett.* **109**, 107002 (2012).

16. Geim, A. K. & Grigorieva, I. V. Van der Waals heterostructures. *Nature* **499**, 419–425 (2013).
17. Burch, K. S., Mandrus, D. & Park, J.-G. Magnetism in two-dimensional van der Waals materials. *Nature* **563**, 47–52 (2018).
18. Idzuchi, H. *et al.* Unconventional supercurrent phase in Ising superconductor Josephson junction with atomically thin magnetic insulator. *Nat. Commun.* **12**, 5332 (2021).
19. Ai, L. *et al.* Van der Waals ferromagnetic Josephson junctions. *Nat. Commun.* **12**, 6580 (2021).
20. Kang, K. *et al.* van der Waals π Josephson Junctions. *Nano Lett.* **22**, 5510–5515 (2022).
21. Hu, G. *et al.* Polarity-reversible zero-field diode effect in van der Waals ferromagnetic Josephson junction for logic operation. *Adv. Mater.* **38**, e13434 (2026).
22. Telford, E. J. *et al.* Layered antiferromagnetism induces large negative magnetoresistance in the van der Waals semiconductor CrSBr. *Adv. Mater.* **32**, 2003240 (2020).
23. Lee, K. *et al.* Magnetic order and symmetry in the 2D semiconductor CrSBr. *Nano Lett.* **21**, 3511–3517 (2021).
24. Wilson, N. P. *et al.* Interlayer electronic coupling on demand in a 2D magnetic semiconductor. *Nat. Mater.* **20**, 1657–1662 (2021).
25. Chen, Y. *et al.* Twist-assisted all-antiferromagnetic tunnel junction in the atomic limit. *Nature* **632**, 1045–1051 (2024).
26. Xi, X. *et al.* Ising pairing in superconducting $NbSe_2$ atomic layers. *Nat. Phys.* **12**, 139–143 (2016).
27. Castellanos-Gomez, A. *et al.* Deterministic transfer of two-dimensional materials by all-dry viscoelastic stamping. *2D Mater.* **1**, 011002 (2014).
28. Zhang, Y., Gu, Y., Li, P., Hu, J. & Jiang, K. General theory of Josephson diodes. *Phys. Rev. X* **12**, 041013 (2022).
29. Jeon, K.-R. *et al.* Zero-field polarity-reversible Josephson supercurrent diodes enabled by a proximity-magnetized Pt barrier. *Nat. Mater.* **21**, 1008–1013 (2022).
30. Díez-Mérida, J. *et al.* Symmetry-broken Josephson junctions and superconducting diodes in magic-angle twisted bilayer graphene. *Nat. Commun.* **14**, 2396 (2023).
31. Wang, D., Wang, Q.-H. & Wu, C. Current-reversion symmetry breaking and the DC Josephson diode effect. *Sci. Bull.* **70**, 4181–4186 (2025).
32. Goldobin, E., Kleiner, R., Koelle, D. & Mints, R. G. Phase retrapping in a pointlike φ Josephson junction: the butterfly effect. *Phys. Rev. Lett.* **111**, 057004 (2013).
33. Zhao, S. Y. F. *et al.* Time-reversal symmetry breaking superconductivity between twisted cuprate superconductors. *Science* **382**, 1422–1427 (2023).
34. Likharev, K. K. Superconducting weak links. *Rev. Mod. Phys.* **51**, 101–159 (1979).
35. Reinhardt, S. *et al.* Link between supercurrent diode and anomalous Josephson effect revealed by gate-controlled interferometry. *Nat. Commun.* **15**, 4413 (2024).
36. Stoutimore, M. J. A. *et al.* Second-harmonic current-phase relation in Josephson junctions with ferromagnetic barriers. *Phys. Rev. Lett.* **121**, 177702 (2018).
37. Kalashnikov, D. S. *et al.* Demonstration of a Josephson vortex-based memory cell with microwave

energy-efficient readout. *Commun. Phys.* **7**, 88 (2024).
38. Wu, H. *et al.* The field-free Josephson diode in a van der Waals heterostructure. *Nature* **604**, 653–656 (2022).
39. Kim, J.-K. *et al.* Intrinsic supercurrent non-reciprocity coupled to the crystal structure of a van der Waals Josephson barrier. *Nat. Commun.* **15**, 1120 (2024).
40. Hamill, A. *et al.* Two-fold symmetric superconductivity in few-layer $NbSe_2$. *Nat. Phys.* **17**, 949–954 (2021).
41. Bauriedl, L. *et al.* Supercurrent diode effect and magnetochiral anisotropy in few-layer $NbSe_2$. *Nat. Commun.* **13**, 4266 (2022).
42. Tschudin, M. A. *et al.* Imaging nanomagnetism and magnetic phase transitions in atomically thin CrSBr. *Nat. Commun.* **15**, 6005 (2024).
43. Hong, C. *et al.* Charge transfer governed interlayer magnetic coupling and symmetry breaking in a van der Waals magnet. *Nat. Commun.* **16**, 9498 (2025).
44. Kamra, A., Rezaei, A. & Belzig, W. Spin splitting induced in a superconductor by an antiferromagnetic insulator. *Phys. Rev. Lett.* **121**, 247702 (2018).
45. Jo, J. *et al.* Local control of superconductivity in a $NbSe_2$/CrSBr van der Waals heterostructure. *Nat. Commun.* **14**, 7253 (2023).
46. Mehrnejat, A. *et al.* Flux-pinning mediated superconducting diode effect in $NbSe_2/CrGeTe_3$ heterostructure. *2D Mater.* **11**, 021002 (2024).
47. Wang, H. *et al.* Quantum superconducting diode effect with perfect efficiency above liquid-nitrogen temperature. *Nat. Phys.* **22**, 47–53 (2026).
48. Lou, H.-X. *et al.* Quantized radio-frequency rectification in a kagome superconductor Josephson diode. *Nat. Nanotechnol.* **21**, 554–560 (2026).

Main figures and captions

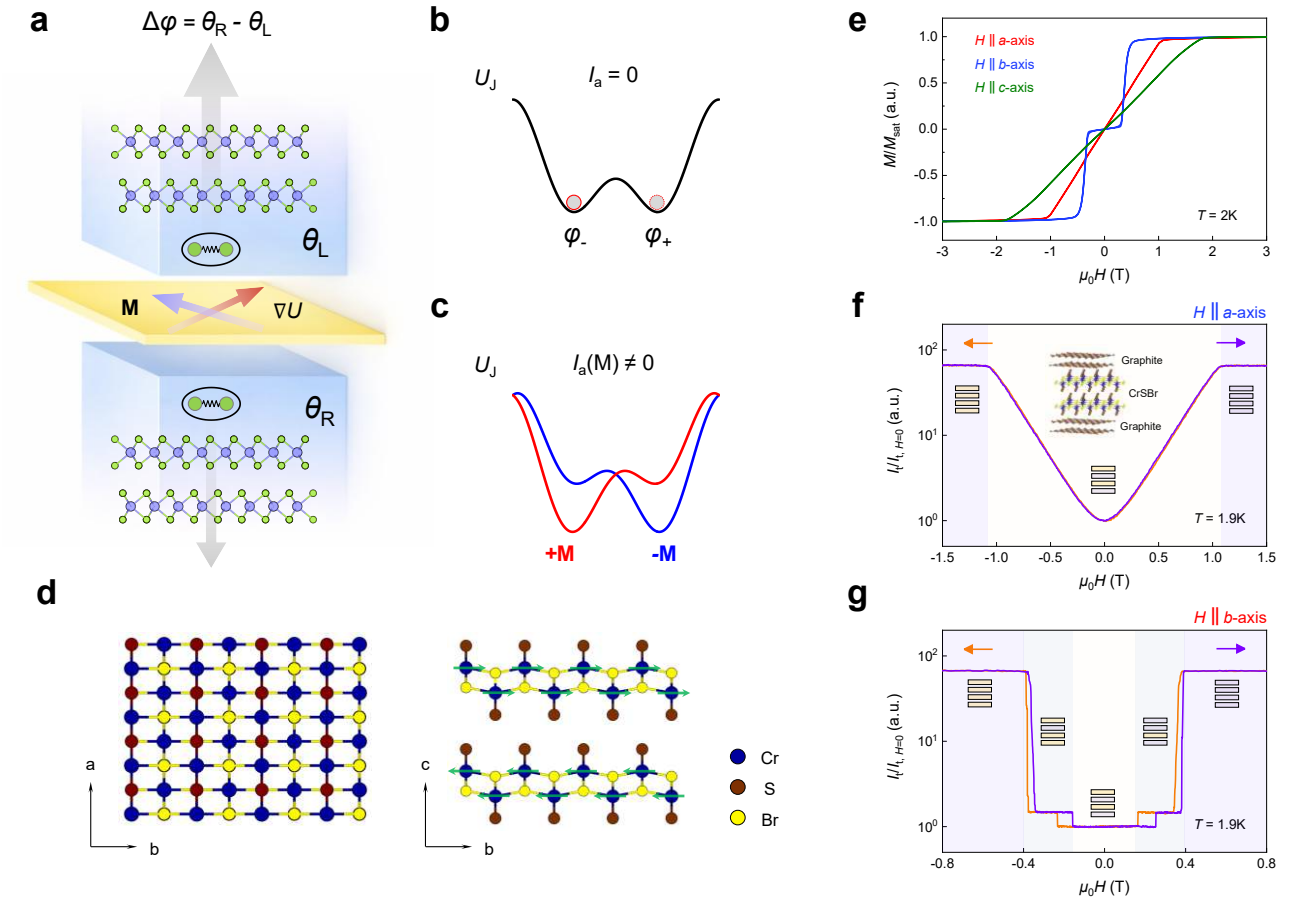


Figure 1. Magnetic control of bistable Josephson phases in layered antiferromagnet CrSBr. a, Schematic of a vertical $NbSe_2$/CrSBr/$NbSe_2$ Josephson junction (JJ), with the superconducting phase difference $\Delta\varphi = \theta_R - \theta_L$ across the magnetic barrier. The magnetization **M** and interfacial potential gradient ∇U illustrate the broken time-reversal and inversion symmetries. **b**, Symmetric bistable Josephson potential U_J for a vanishing magnetization-dependent anomalous contribution ($I_a = 0$), with two phase minima located at φ_- and φ_+, respectively. **c,** Magnetization-dependent potential asymmetry for $I_a(M) \neq 0$. Reversing the magnetic state interchanges the relative depths of the two minima. **d**, Top (left) and side (right) views of the CrSBr crystal structure and antiferromagnetic spin arrangement. **e**, Normalized magnetization M/M_{sat} of bulk CrSBr at 2 K for magnetic fields ($\mu_0 H$) applied along its *a*-, *b*- and *c*-axes, revealing the magnetic anisotropy. **f**, **g**, Field-dependent normalized tunneling current $I_t/I_{t,H=0}$ in a graphite/four layer-CrSBr/graphite junction at 1.9 K, with the field along the *a*-axis (**f**) and *b*-axis (**g**). The continuous response along *a*-axis contrasts with the step-like response along *b*-axis. The arrows mark the field-sweep directions, and the insets illustrate representative magnetic configuration during the field sweeps.

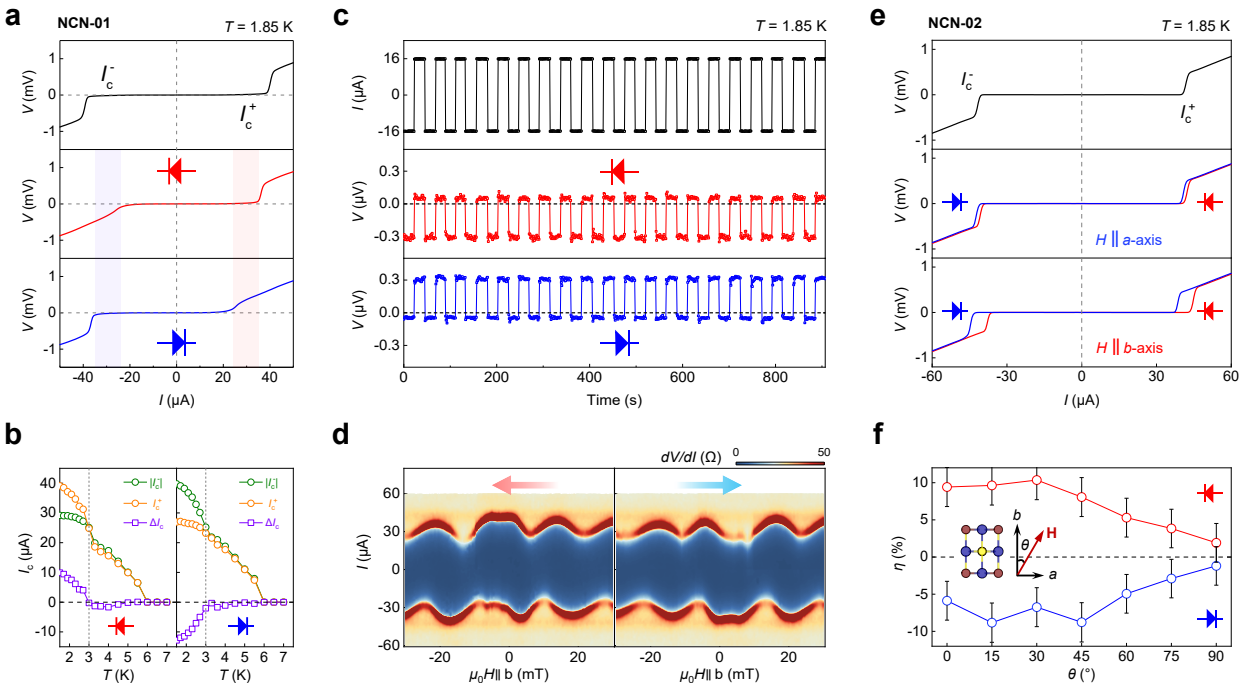


Figure 2. Magnetically reversible zero-field Josephson diode effect in CrSBr-JJs. a, Zero-field current-voltage (IV) characteristics of a four-layer CrSBr-JJ device (NCN-01) at 1.85 K in the untrained state (top) and after opposite magnetic-field training (middle and bottom). The training fields are ± 100 mT. The trained states exhibit reversed asymmetries between the positive and negative switching currents, I_c^+ and $|I_c^-|$, indicating reversal of the JDE polarity. **b**, Temperature (T) dependence of I_c^+, $|I_c^-|$, and $\Delta I_c = I_c^+ - |I_c^-|$ for the two trained magnetic states. The non-reciprocal response weakens with increasing temperature. **c**, Applied alternating square-wave current (top) and the corresponding voltage responses after opposite magnetic training (middle and bottom), demonstrating reversal of the DC rectification polarity. **d**, Differential resistance ($\mathrm{d}V/\mathrm{d}I$) maps of NCN-01 as functions of DC current (I_{DC}) and in-plane magnetic field along the CrSBr b-axis, recorded on downward (left) and upward (right) field sweeps. **e**, Zero-field IV characteristics of a six-layer CrSBr-JJ (NCN-02) before training (top) and after training with fields along the a-axis (middle) and b-axis (bottom), respectively. Training fields of ± 120 mT are used along each axis. **f**, Angular (θ) dependence of the zero-field JDE efficiency η of NCN-02 after opposite magnetic training. The angle θ is defined between the direction of the training field and the CrSBr b-axis. Error bars represent uncertainties in the η propagated from those in switching currents.

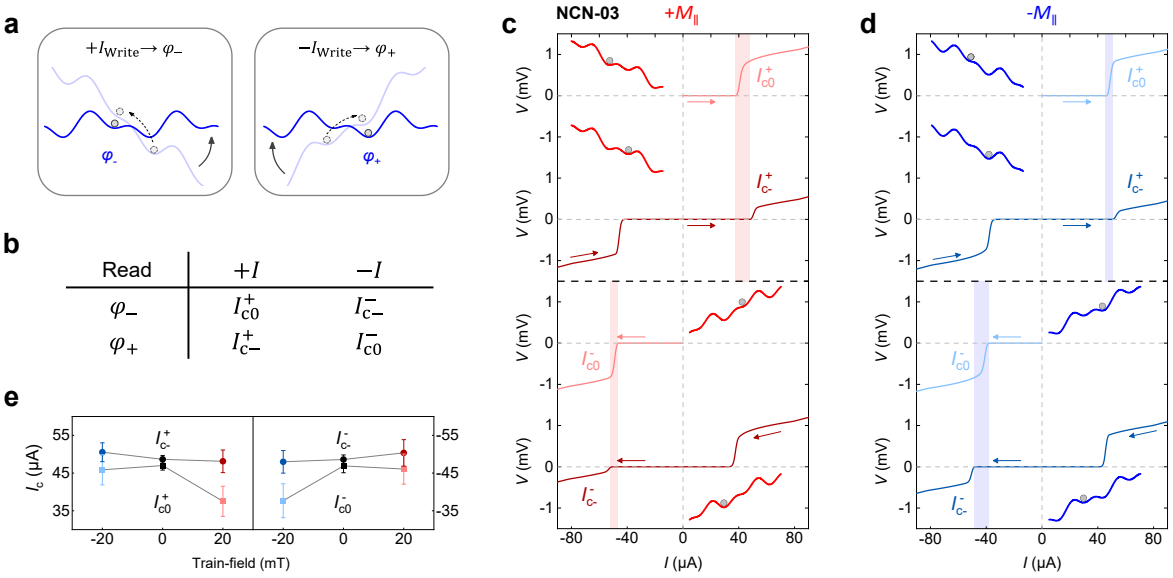


Figure 3. Current-history-dependent switching between inequivalent Josephson branches. a, Schematic of phase-state selection by opposite write-current excursions in a bistable Josephson potential. For the illustrated configuration, positive and negative current histories prepare φ_- and φ_+, respectively. **b**, Correspondence between the occupied phase state and the positive- or negative-current switching branch, $I_{c0}^{\pm}$ or $I_{c-}^{\pm}$. **c**, **d**, Current-history-resolved IV characteristics of the five-layer CrSBr mixed SQUID device (NCN-03) at 1.6 K following opposite in-plane magnetic presets, $+M_{\parallel}$ (**c**) and $-M_{\parallel}$ (**d**). The four traces in each panel distinguish the two switching branches for both current polarities. The arrows indicate the sweep direction, and the shaded regions mark the corresponding differences in the switching thresholds. **e**, Extracted switching currents as a function of magnetic training field.

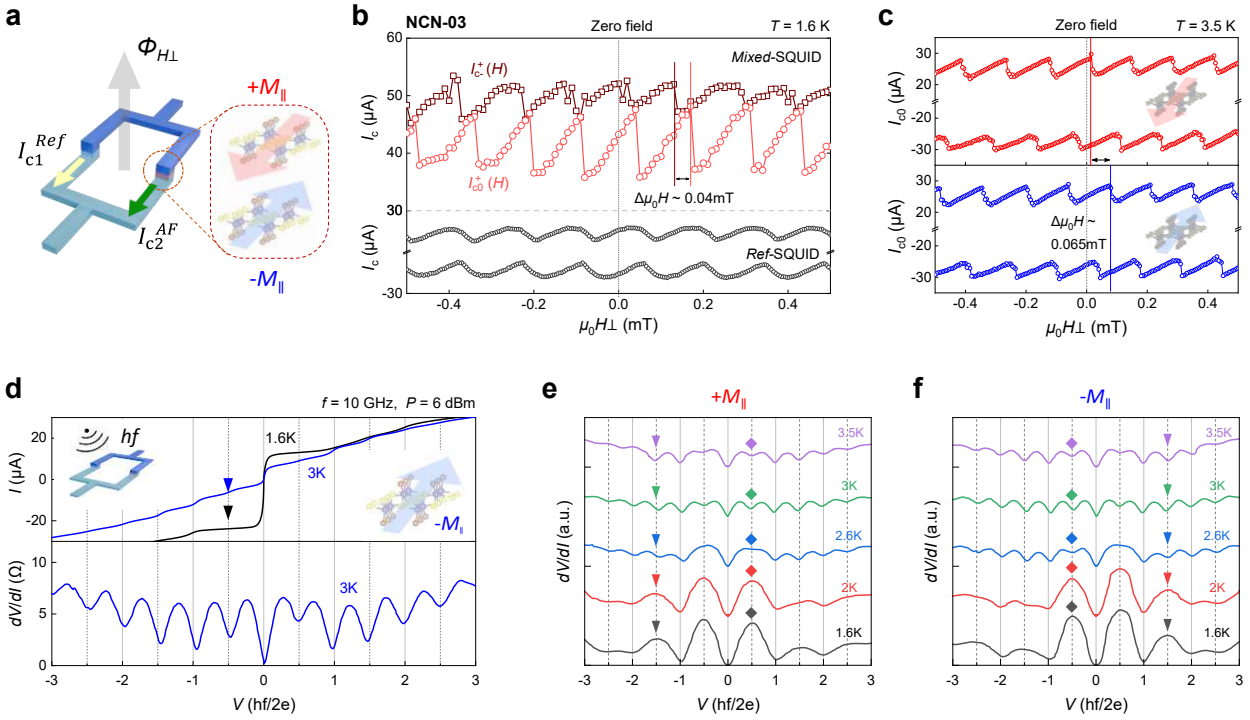


Figure 4. Phase-sensitive interferometry and magnetization-dependent AC Josephson response. **a**, Schematic of the mixed SQUID comprising a CrSBr-JJ and a nonmagnetic reference junction. Opposite remanent magnetic states are initialized by an in-plane field along the CrSBr *b*-axis before out-of-plane SQUID interferometry. **b**, Positive-current switching interference patterns of NCN-03 at 1.6 K after the $+M_{\parallel}$ preset. The I_{c0}^{+} and I_{c-}^{+} branches show an effective field displacement of approximately 0.04 mT, corresponding to a relative interferometric phase offset of $(0.58 \pm 0.11)\pi$. The simultaneously measured all-$NbSe_2$ SQUID (lower) provides an in situ field-reference control. **c**, Interference patterns of the I_{c0} branch at 3.5 K after opposite magnetic presets. Their displacement of approximately 0.065 mT indicates an effective interferometric phase offset of $(0.95 \pm 0.06)\pi$. **d**, Microwave-driven IV characteristics at 1.6 K and 3 K after the $-M_{\parallel}$ preset, measured at frequency $f = 10$ GHz and power $P = 6$ dBm (top), and the corresponding $\mathrm{d}V/\mathrm{d}I$ trace at 3 K (bottom), both plotted against the normalized voltage $V/(hf/2e)$. The half-integer Shapiro features emerge at the elevated temperature. **e**, **f**, Temperature evolution of the normalized $\mathrm{d}V/\mathrm{d}I$ spectra under the same microwave drive after $+M_{\parallel}$ (**e**) and $-M_{\parallel}$ (**f**) training. Their bias-polarity-dependent structures reverse with the magnetic presets, while half-integer features indicate a substantial higher-harmonic contribution to the current-phase relation (CPR).

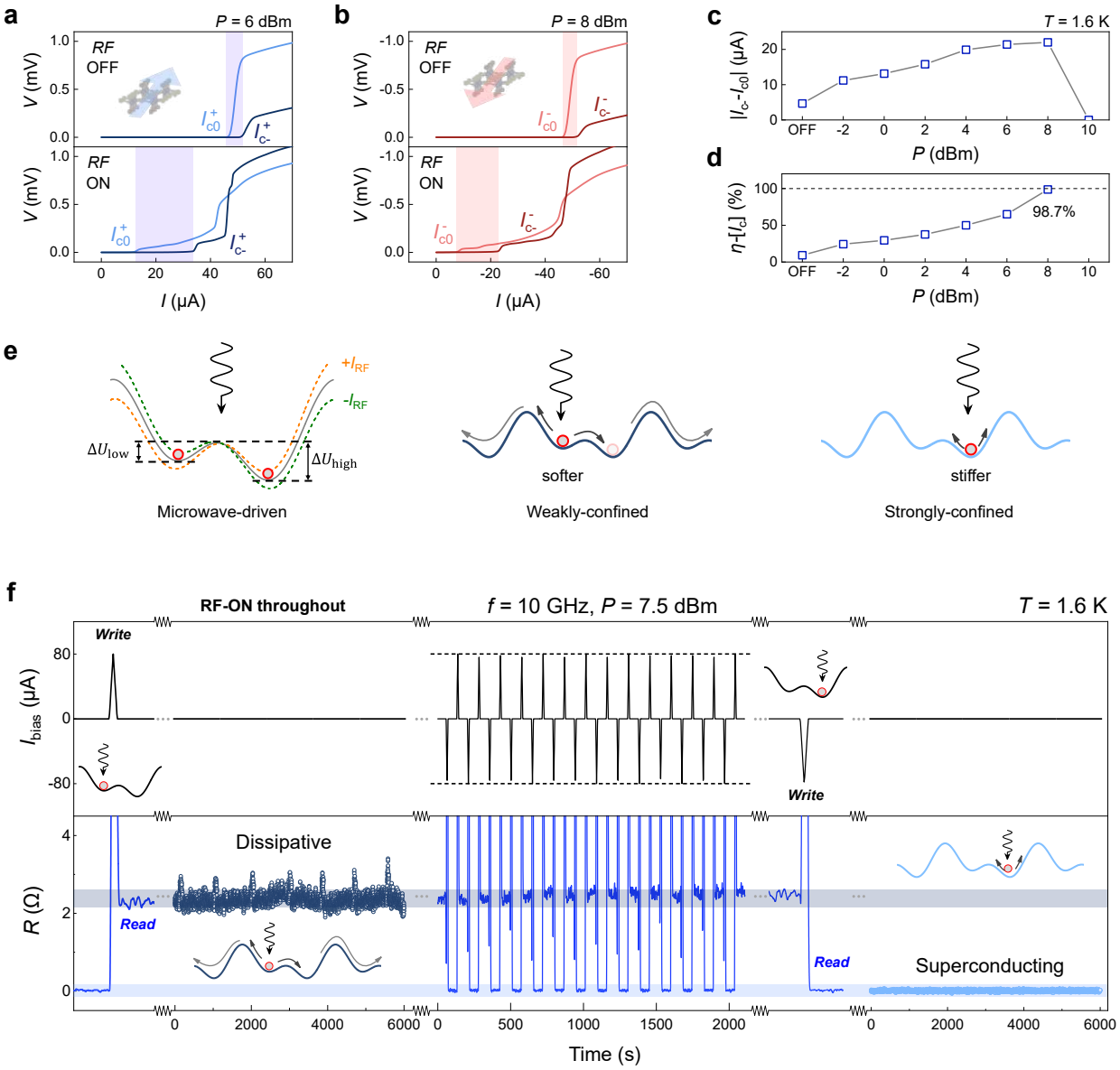
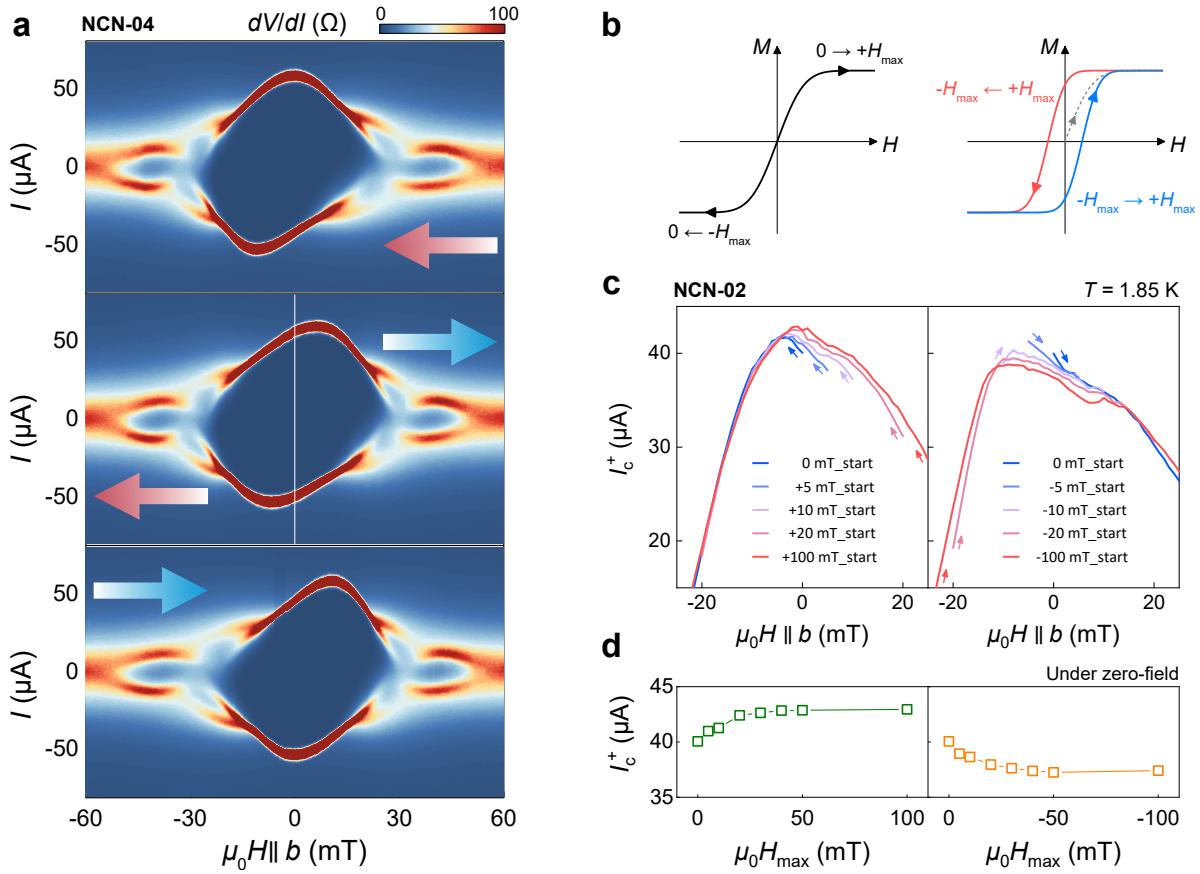
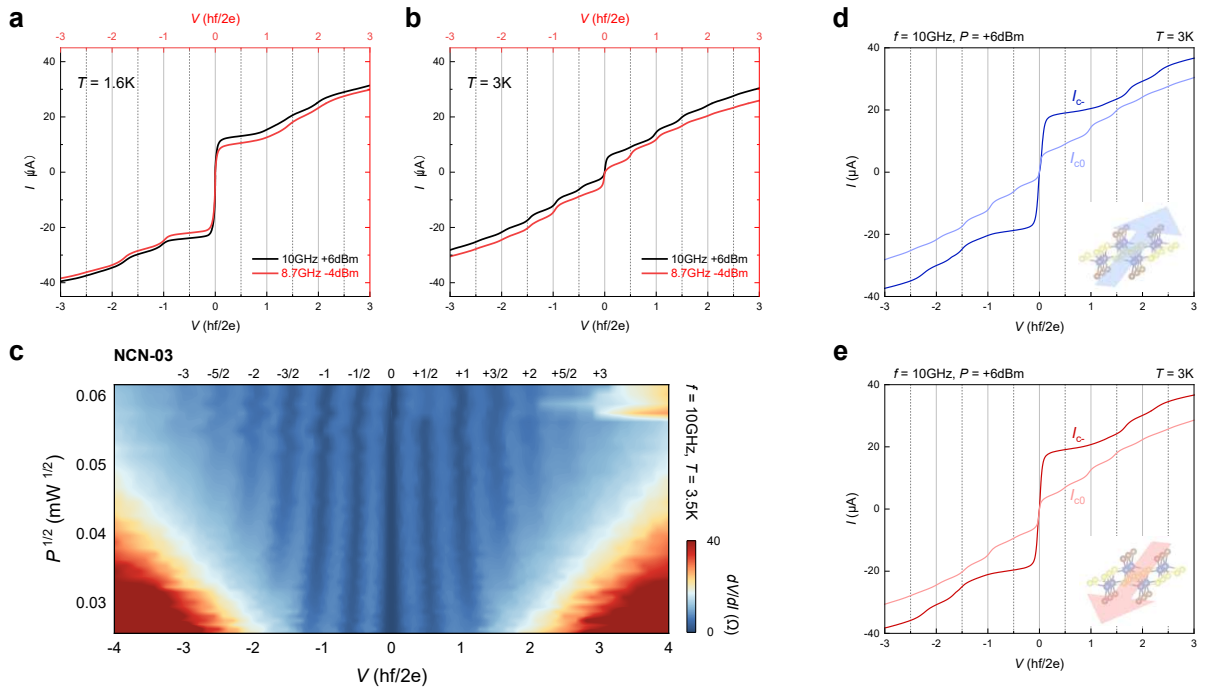


Figure 5. Microwave-enhanced branch contrast and zero-DC-bias readout of phase memory. a, **b**, Representative current-history-resolved IV characteristics of NCN-03 without (top) and with (bottom) microwave irradiation. The positive-current branches after the $-M_{\parallel}$ preset are shown at $P = 6$ dBm (**a**), and the negative-current branches after the $+M_{\parallel}$ preset at $P = 8$ dBm (**b**). **c**, Microwave-power dependence of the absolute branch separation, $|I_{c-} - I_{c0}|$, in the $-M_{\parallel}$ state at 1.6 K. **d,** Corresponding normalized branch contrast, $\eta = |(I_{c-} - I_{c0})/I_{c-}| \times 100\%$. η increases over an intermediate power range and reaches 98.7% at 8 dBm. **e**, Phenomenological illustration of microwave-driven phase dynamics in an asymmetric bistable Josephson potential. The two minima have unequal local stiffnesses and escape barriers, so periodic RF driving can destabilize the more weakly confined state while leaving the more strongly confined state trapped. **f,** Current-write sequence (top) and zero-DC-bias resistance readout (bottom) of NCN-03 at 1.6 K after the $-M_{\parallel}$ preset, with continuous 10 GHz, 7.5 dBm microwave irradiation. The positive write-current excursion prepares a finite-resistance state, whereas the negative excursion restores a near-zero-resistance state. Repeated alternation reproducibly switches between the two resistance states, which remain distinguishable for at least 6000 seconds after removal of the write current.

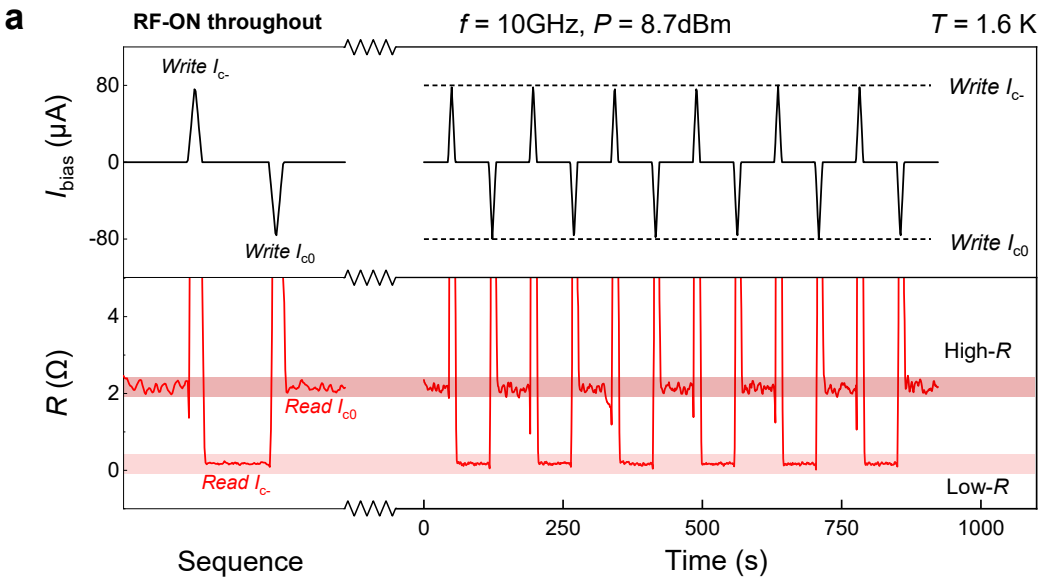
Extended Data



Extended Data Figure 1. Josephson interference modulated by magnetic history. a, $\mathrm{d}V/\mathrm{d}I$ maps of a five-layer CrSBr-JJ device (NCN-04) at 1.85 K for in-plane $\mu_0 H$ applied along the CrSBr *b*-axis. The middle panel shows the initial field excursion after zero-field cooling ($0 \rightarrow \pm\mu_0 H$); the top and bottom panels show results of subsequent field sweeps in opposite directions. The field history produces pronounced hysteretic distortions of the interference pattern. **b**, Schematic magnetization curves illustrating the difference between an initial field excursion and a hysteretic, field-trained magnetic response. **c**, Positive switching current I_c^+ of the six-layer CrSBr-JJ NCN-02 versus *b*-axis field following different positive (left) and negative (right) maximum starting fields, $\mu_0 H_{\mathrm{max}}$, at 1.85 K. Increasing $\mu_0 H_{\mathrm{max}}$ progressively modifies the return-field dependence of I_c^+ before the response approaches saturation. **d**, Zero-field I_c^+ extracted from these sweeps as a function of the training-field amplitude. The response evolves with magnetic history and approaches saturation at sufficiently large fields.

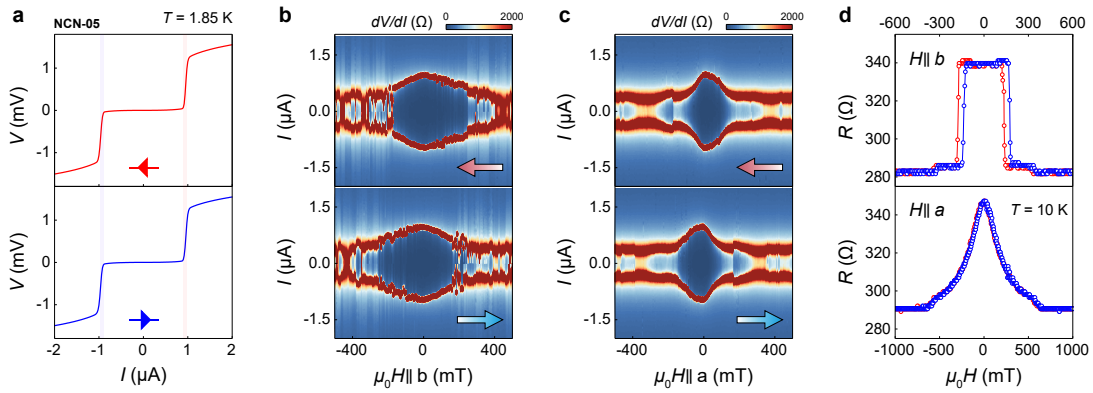


Extended Data Figure 2. Frequency-, power- and branch-dependent Shapiro response. a, **b**, IV characteristics of NCN-03 at 1.6 K (**a**) and 3 K (**b**) after the $+M_{\parallel}$ preset, measured at microwave frequencies of 10 GHz and 8.7 GHz. Integer and half-integer step positions scale with $hf/2e$, identifying their AC Josephson origin. **c**, $\mathrm{d}V/\mathrm{d}I$ maps as a function of normalized voltage and the square root of the applied microwave power for NCN-03 at 3.5 K and 10 GHz in the $+M_{\parallel}$ state. The half-integer features remain at the expected normalized voltages as the drive is varied. **d**, **e**, Branch-resolved Shapiro responses at 3 K under 10 GHz, 6 dBm excitation after $-M_{\parallel}$ (**d**) and $+M_{\parallel}$ (**e**) training. Half-integer structures are more prominent in the I_{c0} branch and strongly suppressed in the $I_{\mathrm{c-}}$ branch.



583

584 **Extended Data Figure 3. Write-read switching after positive-field magnetic preset. a**, Applied
585 write-current sequence (top) and zero-DC-bias resistance (bottom) of NCN-03 at 1.6 K after the
586 $+M_{\parallel}$ preset, with continuous 10 GHz, 8.7 dBm microwave irradiation. Positive and negative
587 write-current excursions address the I_{c-} and I_{c0} branches, producing the low- and high-resistance
588 outputs, respectively. Compared with the $-M_{\parallel}$ preset in Fig. 5, the mapping between write-current
589 polarity and resistance readout is reversed, while the states are repeatedly selected without a DC read
590 bias.



591

592 **Extended Data Figure 4. Magnetically active CrSBr-JJ without a zero-field JDE. a,** Zero-field
593 IV characteristics of a four-layer CrSBr-JJ device (NCN-05) at 1.85 K after opposite magnetic
594 training presets. The switching currents remain nearly reciprocal in both states, showing no zero-field
595 JDE. **b**, **c**, $\mathrm{d}V/\mathrm{d}I$ interference maps under in-plane fields along the CrSBr *b*-axis (**b**) and *a*-axis (**c**).
596 The *b*-axis response exhibits sharp, hysteretic changes, whereas the *a*-axis response evolves more
597 continuously. **d**, Normal-state junction resistance (R) at 10 K, above the superconducting transition
598 temperature, with $\mu_0 H$ applied along the *b*-axis (upper) and *a*-axis (lower). The anisotropic magnetic
599 response persists despite the absence of a detectable zero-field JDE.

Device	Geometry	d (CrSBr) (nm)	Area (Junction) (μm^2)	λ_L ($NbSe_2$) (nm)	J_c (Junction) (A/cm^2)	I_cR_n (Junction) (μV)	Zero-field JDE efficiency (%)	Field training (mT)
NCN-01	JJ	3.1 (4L)	17.4	11.5	221.3	866.3	14.5 (+*M*, *b*-axis) 19.2 (-*M*, *b*-axis)	±100
NCN-02	JJ	4.9 (6L)	19.4	16.1	202.6	318.3	9.4 (+*M*, *b*-axis) 1.9 (+*M*, *a*-axis)	±120
NCN-03	Mixed SQUID	4.2 (5L)	4.7 (CrSBr-JJ) 12.1 (SQUID-empty) 15.0 (SQUID-effective)	—	—	—	11.5 (+*M*, *b*-axis) 10.1 (-*M*, *b*-axis)	±20
NCN-04	JJ	4.0 (5L)	18.6	10.4	266.7	471.2	13.3 (+*M*, *b*-axis) 12.1 (-*M*, *b*-axis)	±120
NCN-05	JJ	3.2 (4L)	10.3	—	8.1	256.1	Zero	±600
WCW-01	JJ	3.9 (5L)	22.8	—	440.4	2028.1	9.1 (+*M*, *b*-axis) 9.2 (-*M*, *b*-axis)	±200

Extended Data Table 1. Device parameters and zero-field JDE efficiency magnitude. Here we summarize the device geometry, CrSBr barrier thickness, junction area, extracted superconducting parameters (including London penetration depth of $NbSe_2$ λ_L extracted from the oscillation period, junction critical current density j_c, junction critical voltage I_cR_n), zero-field JDE efficiency at the base measurement temperature, and field-training amplitude for the CrSBr JJs studied in this work. The zero-field JDE efficiency is defined as

$$|\eta_{JDE}| = \left|\frac{I_c^+ - |I_c^-|}{I_c^+ + |I_c^-|}\right| \times 100\%.$$

Entries for opposite magnetic presets or training-field directions are listed separately when available. NCN-03 has a mixed-SQUID geometry and is used for the phase-sensitive interferometry and branch-resolved microwave measurements. NCN-05 exhibits magnetic hysteresis but no detectable zero-field diode effect. WCW-01 is a control device comprising a WS_2/CrSBr/WS_2 JJ. The comparison separates the reproducible zero-field JDE from measurements that depend on a particular device geometry or excitation protocol.

Supplementary Files

This is a list of supplementary files associated with this preprint. Click to download.

- SupplementaryinformationofPhasehistoryaddressedJosephsonmemorythroughanatomicallythinantiferromagnet.docx